

## **Computational Failure Modeling of Accelerative Injuries to the Lower Leg Below the Knee**

**by Reuben H. Kraft, Megan L. Lynch, Wendy Pino, Aurelie Jean,  
Raul Radovitzky, and Simona Socrate**

**ARL-RP-0421**

**March 2013**

*A reprint from the Proceedings of 2012 ARL Research in Ballistic Protection Technologies,  
May 1–3, 2012 at Aberdeen Proving Ground, MD.*

## **NOTICES**

### **Disclaimers**

The findings in this report are not to be construed as an official Department of the Army position unless so designated by other authorized documents.

Citation of manufacturer's or trade names does not constitute an official endorsement or approval of the use thereof.

Destroy this report when it is no longer needed. Do not return it to the originator.

# **Army Research Laboratory**

Aberdeen Proving Ground, MD 21005

---

**ARL-RP-0421****March 2013**

---

## **Computational Failure Modeling of Accelerative Injuries to the Lower Leg Below the Knee**

**Reuben H. Kraft and Megan L. Lynch**  
**Weapons and Materials Research Directorate, ARL**

**Wendy Pino, Aurelie Jean, Raul Radovitzky, and Simona Socrate**  
**Institute for Soldier Nanotechnologies, Massachusetts Institute of Technology,**  
**Building NE47, Cambridge, Massachusetts 02139**

**A reprint from the *Proceedings of 2012 ARL Research in Ballistic Protection Technologies*,  
May 1–3, 2012 at Aberdeen Proving Ground, MD.**

REPORT DOCUMENTATION PAGE				Form Approved OMB No. 0704-0188	
<p>Public reporting burden for this collection of information is estimated to average 1 hour per response, including the time for reviewing instructions, searching existing data sources, gathering and maintaining the data needed, and completing and reviewing the collection information. Send comments regarding this burden estimate or any other aspect of this collection of information, including suggestions for reducing the burden, to Department of Defense, Washington Headquarters Services, Directorate for Information Operations and Reports (0704-0188), 1215 Jefferson Davis Highway, Suite 1204, Arlington, VA 22202-4302. Respondents should be aware that notwithstanding any other provision of law, no person shall be subject to any penalty for failing to comply with a collection of information if it does not display a currently valid OMB control number.</p> <p><b>PLEASE DO NOT RETURN YOUR FORM TO THE ABOVE ADDRESS.</b></p>					
1. REPORT DATE (DD-MM-YYYY) March 2013		2. REPORT TYPE Reprint		3. DATES COVERED (From - To)	
4. TITLE AND SUBTITLE Computational Failure Modeling of Accelerative Injuries to the Lower Leg Below the Knee				5a. CONTRACT NUMBER	
				5b. GRANT NUMBER	
				5c. PROGRAM ELEMENT NUMBER	
6. AUTHOR(S) Reuben H. Kraft, Megan L. Lynch, Wendy Pino, Aurelie Jean, Raul Radovitzky, and Simona Socrate				5d. PROJECT NUMBER	
				5e. TASK NUMBER	
				5f. WORK UNIT NUMBER	
7. PERFORMING ORGANIZATION NAME(S) AND ADDRESS(ES) U.S. Army Research Laboratory ATTN: RDRL-WMP-B Aberdeen Proving Ground, MD 21005				8. PERFORMING ORGANIZATION REPORT NUMBER  ARL-RP-0421	
9. SPONSORING/MONITORING AGENCY NAME(S) AND ADDRESS(ES)				10. SPONSOR/MONITOR'S ACRONYM(S)	
				11. SPONSOR/MONITOR'S REPORT NUMBER(S)	
12. DISTRIBUTION/AVAILABILITY STATEMENT Approved for public release; distribution unlimited.					
13. SUPPLEMENTARY NOTES A reprint from the <i>Proceedings of 2012 ARL Research in Ballistic Protection Technologies</i> , May 1–3, 2012 at Aberdeen Proving Ground, MD.					
14. ABSTRACT Underbody blasts to vehicles from improvised explosives cause severe injuries to the lower extremities, including bone fracture, ligament tear, and muscle rupture. The process of injury and the effectiveness of vehicle system design strategies to enhance soldier protection remains unclear. In this paper, efforts focused on developing a finite element model of the lower extremities undergoing high strain rate blast-induced deformation leading to injury will be discussed. A hierarchical approach is taken. The process of high strain rate direct axial loading that leads to bone fracture and fragmentation is investigated.					
15. SUBJECT TERMS Finite element modeling, underbody blast, lower extremities					
16. SECURITY CLASSIFICATION OF:			17. LIMITATION OF ABSTRACT  UU	18. NUMBER OF PAGES  24	19a. NAME OF RESPONSIBLE PERSON Megan L. Lynch
a. REPORT Unclassified	b. ABSTRACT Unclassified	c. THIS PAGE Unclassified			19b. TELEPHONE NUMBER (Include area code) (410) 306-3648

# Computational Failure Modeling of Accelerative Injuries to the Lower Leg Below the Knee

Reuben H. Kraft<sup>a,1</sup>, Megan L. Lynch<sup>a</sup>, Wendy Pino<sup>b</sup>, Aurelie Jean<sup>b</sup>, Raul Radovitzky<sup>b</sup>,  
Simona Socrate<sup>b</sup>

<sup>a</sup> *Soldier Protection Sciences Branch, U.S. Army Research Laboratory, ATTN: RDRL-WMP-B,  
Aberdeen Proving Ground, Maryland 21005*

<sup>b</sup> *Institute for Soldier Nanotechnologies, Massachusetts Institute of Technology, Building NE47,  
Cambridge, Massachusetts 02139*

## Abstract

Underbody blasts to vehicles from improvised explosives cause severe injuries to the lower extremities, including bone fracture, ligament tear, and muscle rupture. The process of injury and the effectiveness of vehicle system design strategies to enhance soldier protection remains unclear. In this paper, efforts focused on developing a finite element model of the lower extremities undergoing high strain rate blast-induced deformation leading to injury will be discussed. A hierarchical approach is taken. The process of high strain rate direct axial loading that leads to bone fracture and fragmentation is investigated.

---

<sup>1</sup>Corresponding author email: reuben.h.kraft.civ@mail.mil

# Contents

<b>1</b>	<b>Introduction</b>	<b>3</b>
<b>2</b>	<b>Computational Methodology</b>	<b>4</b>
<b>3</b>	<b>Results and Discussion</b>	<b>8</b>
<b>4</b>	<b>Conclusions and Future Work</b>	<b>13</b>

# List of Figures

1	(a) A three-dimensional finite element volume mesh with details of the validation hierarchy for the lower extremities based on the method of Thacker et al. [2007]. The system is decomposed into components, subassemblies, assemblies and system-level models. (a) Lower leg model geometry, and (b) applied velocity. .	5
2	Schematic showing the elastic-fracture constitutive model used to capture fracture. In tension, first there is an linear elastic response until a critical stress, $\sigma_c^t$ , is reached within the element, then linear stress softening occurs until the element critical crack opening stretch, $\epsilon_c^t$ , is reached. In compression, element fails at stress $\sigma_c^c$ . . . . .	6
3	Minimum principal stresses predicted in the mid-tibia for the 3.2 m/s and 17 m/s loading cases. Also shown is the mass removed from simulations as a result of failure. . . . .	9
4	Predicted fracture morphologies for boundary condition (a) 3.2 m/s and (b) 17.5 m/s.	10
5	Maximum compressive stress in the axial direction as a function of time for case of (a) 3.2 and (b) 17.5 m/s. . . . .	10
6	Principal stresses in the plantar surface of the calcaneus and inferior talus for both (a) case 1 and (b) case 2. . . . .	11
7	Damage predicted for the 17.5 m/s impact case over various times . . . . .	12
8	Percentage of mass removed from the simulation for talus for the (a) 3.2 m/s and (b) 17.5 m/s cases. The talus is interesting to examine because this is where damage is first observed. . . . .	13
9	Maximum compressive principal stress plotted in terms of varying tensile critical inelastic stretch, $\epsilon_i$ for the 17.5 m/s loading condition. Also shown is the corresponding total mass removed from the system as a result. . . . .	14

# List of Tables

1	Compilation of various constitutive models and parameters used for the lower leg simulation. E is the Young's Modulus, $\nu$ is Poisson's ratio, K is the bulk modulus, $\mu$ is the shear modulus, $K_{IC}$ is the mode-I fracture toughness, $\sigma_c^t$ and $\sigma_c^c$ are the critical failure stresses in tension and compression, respectively, $\epsilon_i$ is the inelastic energy dissipative stretch, $\rho$ is the density and $m$ is mass. . . . .	7
---	---	---

# 1 Introduction

Improvised explosive devices (IEDs) oftentimes hidden along roads and detonated underneath trucks or tanks pose a major threat to soldiers and can cause significant accelerative injuries. The explosion beneath the vehicle is commonly referred to as an underbody blast (UBB) event. It has been reported that 8,159 IED incidents occurred in Afghanistan in 2009, which was an increase from 3,867 and 2,677 which were reported in 2008 and 2007, respectively [Whitlock, 2010]. While civilian car traffic accidents are in the range of 5 to 35 G [Gabauer and Gabler, 2008], an underbody blast may cause accelerations in the lower extremities in the range of 155 to 217 G [Nilakantan and Tabiei, 2009]. During an underbody blast event, within 0.5 ms of the initiation of the explosion a shock wave hits the bottom plate of the vehicle and causes a rapid rise in pressure. This pressure results in local acceleration and subsequent deformations of the plate which apply significant loads to the soldier's lower extremities [NATO HFM-090, Task Group 25, 2007]. As the blast wave reflects under the vehicle, a pressure force acts on the bottom of the vehicle and causes it to lift off the ground. The acceleration of the vehicle and the collisions that follow are also a significant source of injury, especially if the soldier is not properly restrained. In summary, the body is subjected to both the local effects (caused by shock and high rate deformation of the vehicle) and global effects (vehicle motion over time) as a result of the mine detonation process. The local effects are less understood and lead to a range of injuries including fractures of the knee-thigh-hip complex, calcaneus, ankle, midfoot, tibia and fibula shaft and malleoli, as well as knee and other ligament tears and ruptures.

Some of the understanding for injuries experienced within the underbody blast environment can be obtained from the civilian vehicle crash environment. For example, fractures of the ankle and lower foot which are predominant within the military environment, have already been studied to some degree in the past. Manning et al. [1998] report that calcaneal, talar, midfoot and various other ankle fractures have been attributed to the mechanism of axial loading through the plantar surface of the foot. While these injuries might be expected from axial loading, Crandall et al. [2003] demonstrated that even malleolar fractures can occur from pure dynamic axial loading of the leg. Begeman and Paravasthu [1997] also conducted experimental impact tests where unembalmed cadaveric legs were subjected to a uniaxial plantar surface load along the axis of the tibia. Pilon and calcaneal fractures were observed with an average tibial axial force of 7590 N at failure. Kuppa et al. [2001] offers a useful review of calcaneus, talus, ankle and midfoot fracture research, most of which was conducted on postmortem human subjects. While this past research highlights some common features with military blast injuries, it is important to note that the rate of loading to the lower extremities may be 10 – 100 times greater than civilian vehicular crashes. Thus, there is a strong possibility that different injury mechanisms may be activated during these events and new or enhanced injury criteria may be required.

There have been attempts to computationally model underbody blast effects in the lower extremities. Nilakantan and Tabiei [2009] attempted to assess injury by measuring tibia compressive loads following an underbody blast event using finite element analysis of a HYBRID III human surrogate. They make clear that more advanced and biofidelic lower extremity finite element models are needed. Many lower extremity studies employ a combined experimental and simulation-based approach. For example, Manseau and Keown [Manseau and Keown, 2005] compared a physical lower leg model and a computer model in the development of enhanced injury assessment methods, with a focus on the ankle complex and its connections to the tibia. Bandak et al. [2001] developed

an anatomically realistic finite element model of the lower leg to study the effects of axial impact loading to the plantar surface of the foot. The model included explicitly represented bones, cortical and trabecular bone types, and various soft tissues. The plantar surface of the foot was impacted by a rubber-layered plate within a range of velocities up to 6.7 m/s. The model was compared to a set of experiments in which human cadaveric lower legs were impacted by a swinging pendulum at various initial velocities ranging from 2.2 m/s to 7.6 m/s [Yoganandan et al., 1995, 1996]. In the experiments, bone fracture was observed in the distal tibia and calcaneus at velocities at and above 6.7 m/s. The simulations by Bandak et al. [2001] compared reasonably well with the experimental data of Yoganandan et al. [1995, 1996], though an over-prediction in peak load values at the proximal end (i.e. knee) and plantar surface of the foot became increasingly pronounced with increasing velocity (4.47m/s and above), perhaps because failure was not incorporated into the finite element model.

In this paper we develop a numerical model of the lower leg, constructed in an effort to understand the dynamic failure of the lower extremities when subjected to underbody blast loading. This body region (from the knee down) is the area most often injured in an underbelly blast event [Alvarez, 2011], and as such is an important area of study. Three-dimensional, Lagrangian finite element analysis is used [Belytschko et al., 2000]. One long-term objective of this research is to have the capability to provide uncertainty quantification and robust validation for an intact lower extremity model with which to study underbody blast effects. For this reason we adopt the method of Thacker et al. [2007] who used a hierarchical methodology for creating a numerical model of the spine. This paper documents our initial efforts in building the computational framework required for such a hierarchical approach, inspiring both smaller and larger length scale studies (i.e. for the tibia and full leg, respectively) as the objects of future work.

## 2 Computational Methodology

Thacker et al. [2007] provide a useful hierarchical verification and validation scheme that decomposes a system level model into components, subassemblies and assemblies. Within the validation and verification scheme, the process should start at smaller length scales, such as the components, and progress to the last stage of system-level models. This approach requires simulations and experiments to be conducted at each level. While the current research effort adopts the approach proposed by Thacker et al. [2007], we note that this study is a work-in-progress and is still in an early stage of development, where we are identifying the necessary infrastructure and research teams to support both the experimental and numerical modeling efforts at the multiple length scales required. Nevertheless, we begin to define the subdivisions for the lower extremities for this effort and to also help pave the way for future work. The lower extremity system is partitioned into components (ligaments, muscles, cortical and trabecular bone, skin), subassemblies (joints), assemblies (motion segments consisting of muscles, joints, bones) and system level (whole leg) models as depicted in Figure 1a. In accordance with our hierarchical validation and verification strategy, one assembly within the full lower extremity model, the lower leg of the region distal (below) the knee is considered here.

Twenty-eight bones are explicitly represented, to include the tibia, fibula, and the twenty-six bones of the foot [Hall, 2006]. The tibia, fibula, talus, and calcaneus are constructed as layered thin-walled structures to represent cortical and trabecular bone types. The bones of the mid- and



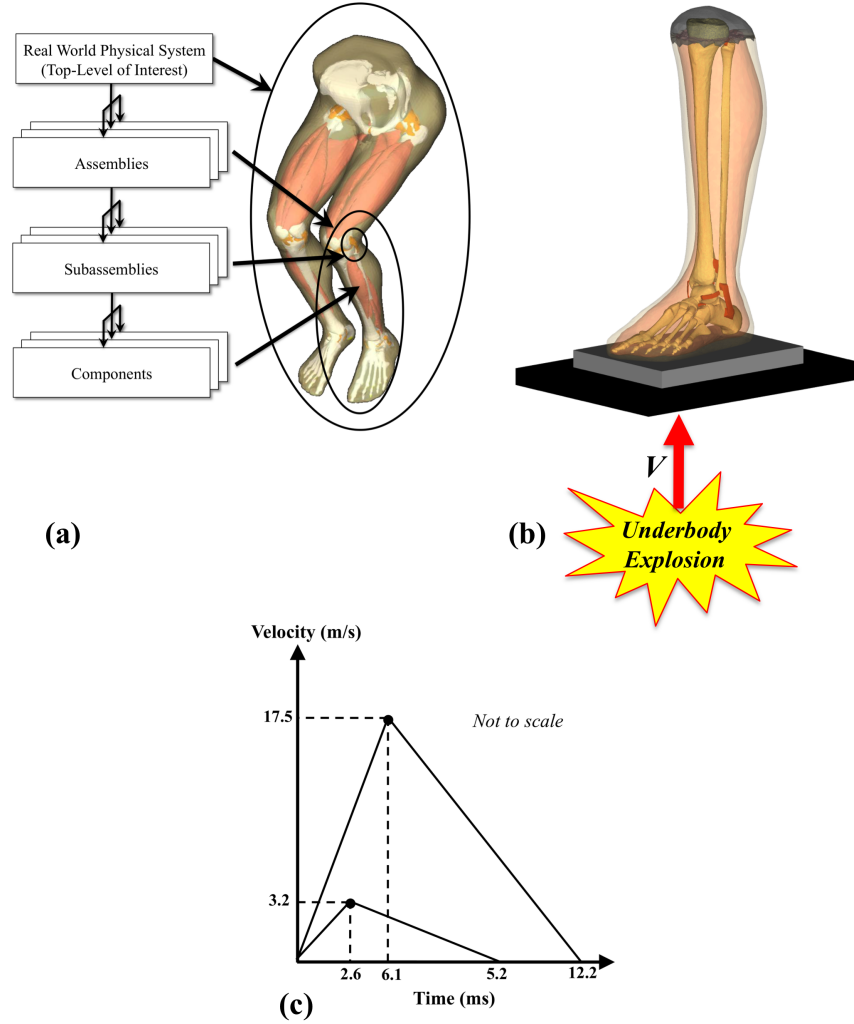


Figure 1: (a) A three-dimensional finite element volume mesh with details of the validation hierarchy for the lower extremities based on the method of Thacker et al. [2007]. The system is decomposed into (a) components, subassemblies, assemblies and system-level models. (b) Lower leg model geometry in assembly model of leg below the knee, and (c) applied velocity boundary conditions used in this study.

forefoot are not segmented into different bone types and are assigned cortical bone properties throughout and have the ability to articulate. Soft tissue and a separate skin layer surround the skeletal structure. The soft tissue, hereby referred to as *bulk tissue* is a homogenization of muscles, tendons, connective tissue, blood vessels, *etc.* using an approach similar to that proposed by Cheung et al. [2005]. The bulk tissue also fills the gaps between bones so that joint structures such as cartilage, bursae, synovial fluid, *etc.* are not explicitly represented. Eight ligaments, however, are explicitly represented in the model and are detailed in Figure 1b. The proximal (top) end of the lower leg is “potted” in a ballast mass as was done by Bandak et al. [2001]. The bottom of the foot contacts a layer of rubber attached to a steel plate. This rubber-plate arrangement was also used by Yoganandan et al. [1995, 1996] and Bandak et al. [2001] as a means of applying load to

the bottom of the foot, and is hereby referred to as the *impactor*. The impactor can also be likened to a boot sole in contact with the floor of a military vehicle, though in this study the rubber is tied to the plate. The anatomical geometry for the model was obtained from Zygote Media Group, Inc. [2012] who created anatomical geometry from CT scans of human specimens who anthropometrically fitting within the 50th percentile Zygote Media Group, Inc. [2012]. The mesh is comprised of 1.53 million 10-noded tetrahedral elements and the long axis of the tibia is aligned with the z-direction, sometimes referred to as the axial direction. Table 1 provides details on the material models and parameters used.

Both cortical and trabecular bone failure is captured within the simulations using simplistic failure models as schematically depicted in Figure 2. In tension, the material behaves as a linear

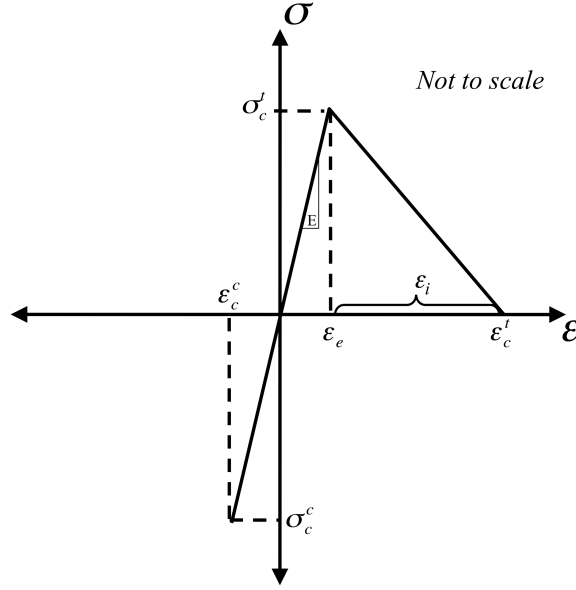


Figure 2: Schematic showing the elastic-fracture constitutive model used to capture fracture. In tension, first there is an linear elastic response until a critical stress,  $\sigma_c^t$ , is reached within the element, then linear stress softening occurs until the element critical crack opening stretch,  $\epsilon_c^t$ , is reached. In compression, element fails at stress  $\sigma_c^c$ .

elastic material until a critical stress,  $\sigma_c^t$ , is reached within an element at strain  $\epsilon_e$ . Then, energy dissipation associated with the fracture process is modeled using linear stress softening until the element strain reaches a critical value,  $\epsilon_c^t$ , at which point the element's mass is also removed from the system. Note that the critical value of strain includes both elastic and inelastic contributions, i.e.,  $\epsilon_c^t = \epsilon_e + \epsilon_i$ , where  $\epsilon_i$  is the inelastic dissipative strain. The slope of the stress softening curve should be scaled so that the energy dissipated by the degraded element equals the fracture energy of a crack passing through the element, thereby rendering the solution relatively mesh size independent [Song et al., 2008, Donadon et al., 2008, Cervera and Chiumenti, 2006, Iannucci and Willows, 2006]. To obtain energy equivalence for a degraded element obeying the stress-strain law shown in Figure 2, the following relation should be met:

$$G_f A = \frac{1}{2} E \epsilon_e \epsilon_i V^e \quad (1)$$

Table 1: Compilation of various constitutive models and parameters used for the lower leg simulation.  $E$  is the Young's Modulus,  $\nu$  is Poisson's ratio,  $K$  is the bulk modulus,  $\mu$  is the shear modulus,  $K_{IC}$  is the mode-I fracture toughness,  $\sigma_c^t$  and  $\sigma_c^c$  are the critical failure stresses in tension and compression, respectively,  $\varepsilon_i$  is the inelastic energy dissipative stretch,  $\rho$  is the density and  $m$  is mass.

Anatomic Component	Material Model	Material Properties	References
Bone	Cortical bone	Elastic with maximum principal stress-based fracture model $E = 19.0 \text{ GPa}$ $\nu = 0.3$ $K_{IC} = 7 \text{ MPa}\sqrt{m}$ $\sigma_c^t = 132 \text{ MPa}$ $\varepsilon_i = 0.022$ $\sigma_c^c = -396 \text{ MPa}$ $\rho = 1810 \text{ kg/m}^3$	Bandak et al. [2001] Schuster et al. [2000] Ural et al. [2011] Currey [2002]
	Trabecular bone	Elastic with maximum principal stress-based fracture model $E = 300 \text{ MPa}$ $\nu = 0.45$ $K_{IC} = 0.4 \text{ MPa}\sqrt{m}$ $\sigma_c^t = 1.5 \text{ MPa}$ $\varepsilon_i = 0.230$ $\sigma_c^c = -4.5 \text{ MPa}$ $\rho = 600 \text{ kg/m}^3$	Schuster et al. [2000] Cook and Zioupos [2009]
Ligaments	Neo-Hookean	$K = 250 \text{ MPa}$ $\mu = 5.0 \text{ MPa}$ $\rho = 1040 \text{ kg/m}^3$	Bandak et al. [2001]
Skin	Neo-Hookean	$K = 333 \text{ MPa}$ $\mu = 6.7 \text{ MPa}$ $\rho = 1040 \text{ kg/m}^3$	Bandak et al. [2001]
Bulk Muscle	Neo-Hookean	$K = 333 \text{ MPa}$ $\mu = 6.7 \text{ MPa}$ $\rho = 1040 \text{ kg/m}^3$	Bandak et al. [2001]
Rubber Layer	Elastic	$E = 1.0 \text{ GPa}$ $\nu = 0.4$ $\rho = 1000 \text{ kg/m}^3$	
Plate	Elastic	$E = 190.0 \text{ GPa}$ $\nu = 0.28$	MatWeb [2011]
		$m = 24.5 \text{ kg}$	Bandak et al. [2001]
Knee Ballast Mass	Elastic	$E = 190.0 \text{ GPa}$ $\nu = 0.28$	MatWeb [2011]
		$m = 11.3 \text{ kg}$	Bandak et al. [2001]

where  $G_f$  is the fracture energy of the material per unit area,  $A$  is the fracture area of a crack passing through the element,  $E$  is Young's Modulus, and  $V^e$  is the volume of the element. In the current study,  $G_f$  is determined using the elastic fracture mechanics relation  $K_{Ic}^2 = E'G_f$ , where  $K_{Ic}$  is the mode-I fracture toughness of the material. Therefore, in plane stress where  $E' = E$ ,

$G_f$  was determined to be 2578 J/m<sup>2</sup> and 533 J/m<sup>2</sup> for cortical and trabecular bone, respectively, using the values listed in Table 1. Both  $A$  and  $V^e$  in Equation 1 are mesh parameters. Assuming regular tetrahedral elements in which all edge lengths,  $a$ , are equal,  $V^e = (\sqrt{2}/12)a^3$ . Also assuming a flat crack face passing through two nodes of the tetrahedron and bisecting the opposite edge, the fracture surface is obtained as  $A = (\sqrt{2}/4)a^2$ . To satisfy Equation 1, the value of  $\varepsilon_i$  is adjusted in the elastic-fracture material model for both cortical and trabecular bone.

In the current mesh, a distribution of element aspect ratios and sizes exist, which contributes to a range of element volumes  $V^e$  ( $2.62 \times 10^{-11}$  to  $1.70 \times 10^{-8}$  m<sup>3</sup> for cortical bone,  $2.40 \times 10^{-10}$  to  $9.36 \times 10^{-8}$  m<sup>3</sup> for trabecular bone) and corresponding fracture areas  $A$ . Given this variability, and still assuming regular tetrahedral elements,  $\varepsilon_i$  has a range of 0.193 to 0.022 for the smallest and largest elements of cortical bone, respectively. For trabecular bone,  $\varepsilon_i$  has a range of 1.683 to 0.230 for the smallest and largest elements, respectively. In this study we consider how these ranges of inelastic strain parameters influence the predicted values of stress and damage in the lower extremities, but first we establish a benchmark simulations using the maximum element length scales. The inelastic dissipative strain for both cortical and trabecular bone is given by:

*Cortical bone:*

$$\varepsilon_i = \frac{2G_f A}{\sigma_c^t V^e} = \frac{2(2578 \text{ J/m}^2)(9.72 \times 10^{-6} \text{ m}^2)}{(132 \text{ MPa})(1.70 \times 10^{-8} \text{ m}^3)} \approx 0.022 \quad (2)$$

*Trabecular bone:*

$$\varepsilon_i = \frac{2(533 \text{ J/m}^2)(3.03 \times 10^{-5} \text{ m}^2)}{(1.5 \text{ MPa})(9.36 \times 10^{-8} \text{ m}^3)} \approx 0.230 \quad (3)$$

Compressive failure in both cortical and trabecular bone is captured using a minimum principal stress failure criterion and artificial element deletion: Energy is not dissipated by the constitutive model once the element reaches its failure criterion and its mass is simply removed from the system upon deletion. As shown in Figure 2, no stress softening curve is present past the failure criterion,  $\sigma_c^c$ , because the elastic-fracture material model used in this study currently does not support it. Adding this capability will be the focus of future work.  $\sigma_c^c$  for both cortical and trabecular bone is determined by  $\sigma_c^c = -3\sigma_c^t$ .

A variety of boundary conditions have been investigated. Figures 1c and d show the range of velocity profiles applied to the plate in this study, all in the positive  $z$ -direction. The 17.5 and 3.2 m/s velocity profiles (Figure 1c) are considered baselines. In all cases the plate is fixed in the  $x$  and  $y$  directions. A gravity setting with a gravitational constant of 9.8 m/s<sup>2</sup> has been applied in the negative  $z$ -direction. The ballast mass is fixed in the  $x$  and  $y$  directions.

### 3 Results and Discussion

Figure 3 shows the evolution of minimum principal stress predicted by the computations at the mid-tibia. For the tibia response, both tensile and compressive stresses were examined to predict failure; however, the tensile component is small in magnitude compared to the compressive component and is not shown in the figure. The compressive stresses reach a peak value of approximately -58 MPa for the 17.5 m/s case (case 2) at approximately 3.2 ms; for the 3.2 m/s case (case 1), peak stress is approximately -38 MPa at 3.8 ms. The percentage of bone damage is also shown in Figure 3. A quick estimate of damage to the various bones can be obtained from the percentage of mass

removed from the system. As detailed in Section 2, for tensile failure the mass of fully degraded elements is zeroed, while for compressive failure direct element deletion is used. For the 17.5 m/s case, numerical instabilities occur at a total percentage of bone damage equal to 11.5%; for the 3.2 m/s case, numerical instabilities occur at a total percentage of bone damage equal to 13.5%. This total bone damage will be decomposed into individual components and discussed in more detail shortly. Interestingly, for case 2 the foot stays in direct contact with the rubber surface and experiences significant comminution and failure - the decrease in stress magnitude in the mid tibia, illustrated in Figure 3, is due to degradation in the ability to carry load. However, for case 1, while some failure is predicted much of the stress drop in the tibia is due to unloading of the lower leg because of separation of the foot-rubber interface (sometimes referred to as liftoff) and movement of the ballast mass at the top of the lower leg assembly.

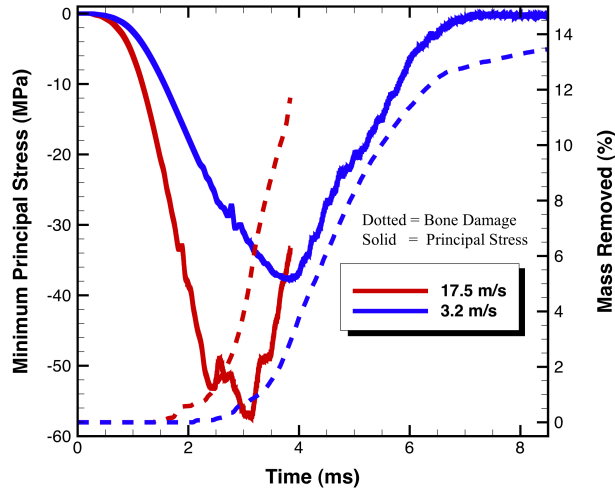


Figure 3: Minimum principal stresses predicted in the mid-tibia for the 3.2 m/s and 17 m/s loading cases. Also shown is the mass removed from simulations as a result of failure.

Figure 4a and b show the bone structures at the end of the simulations for the two load cases shown in Figure 1c. A single calcaneus fracture is seen for case 1, while for case 2, massive comminution of the calcaneus is observed. Fracture of the talus, distal tibia and comminuted fracture of the calcaneus is also predicted. In both cases, no mid-shaft tibia fractures are predicted. Interestingly, the arrows in Figures 4a and b shows an example of how the dynamic fracture process is different between the two different loading rates. In case 1, at the lower strain rate, no dynamic crack branching was predicted, however in case 2 crack bifurcation is predicted. This type of information would be useful to the armor designer or medical team because these injuries require different treatment approaches. In case 1 a relatively simple fracture is predicted, while at higher rates bone fragmentation is expected.

Figure 5a and b shows the global minimum stress in the axial direction in the tibia, talus and calcaneus as a function of time. For case 1 the compressive stress in the tibia, talus and calcaneus reach approximately -60 MPa within approximately 2.0 ms of impact. At approximately 2.0 ms the rate of growth of the compressive stress within the talus increases and stresses reach a maximum value of approximately -200 MPa at 3.9 ms followed by unloading. The increase in talus compression stress occurs just as elements in the talus begin to undergo deletion due to material

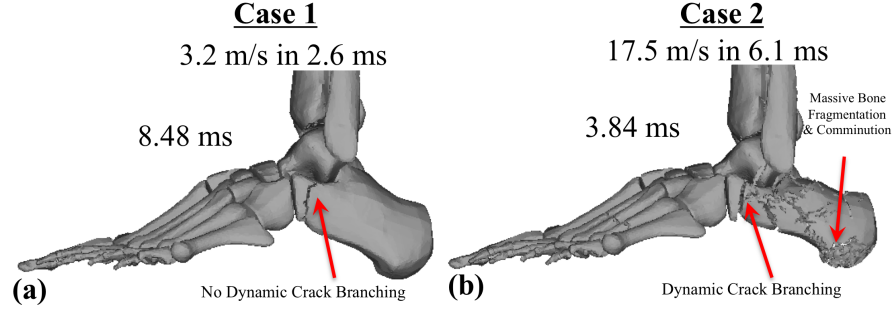


Figure 4: Predicted fracture morphologies for boundary condition (a) 3.2 m/s and (b) 17.5 m/s.

failure (at 2.0 ms). The tibia response also shows a sharp increase in axial stress level at approximately 2.6 ms, followed by a gradual stress increase to a maximum of -375 MPa at 4.5 ms, and subsequent unloading. The calcaneus response shows a dramatic increase in compressive stress at approximately 5.2 ms when the axial stress reaches the compressive failure criterion of -396 MPa. Typically, these conditions indicate that a crushing mode has been reached in the bone. However, given that the foot is entering into an unloading state (as indicated by the displacement of the ballast, the dashed line in Figure 5a) numerical instabilities might play a role in these results, which should be therefore regarded with some level of caution. Despite these considerations, for both the 3.2 and 17.5 m/s cases damage starts first in the talus. Reflecting waves induce localized regions of tensile stress where cracks can initiate. In addition, the calcaneus is somewhat protected by its ability to rotate counterclockwise about the talus in the sagittal plane while the tibia is able to withstand higher levels of imposed distal displacements as the strain is distributed over its considerable length. Conversely, the talus is tightly constrained between the rotating calcaneus and the tibia. For the 17.5 m/s case, the response at times less than 1.5 ms is qualitatively similar to the lower rate case, with analogous patterns of stress growth in the tibia, talus and calcaneus. Unfortunately, numerical instabilities are observed in all three regions as the transient analysis.

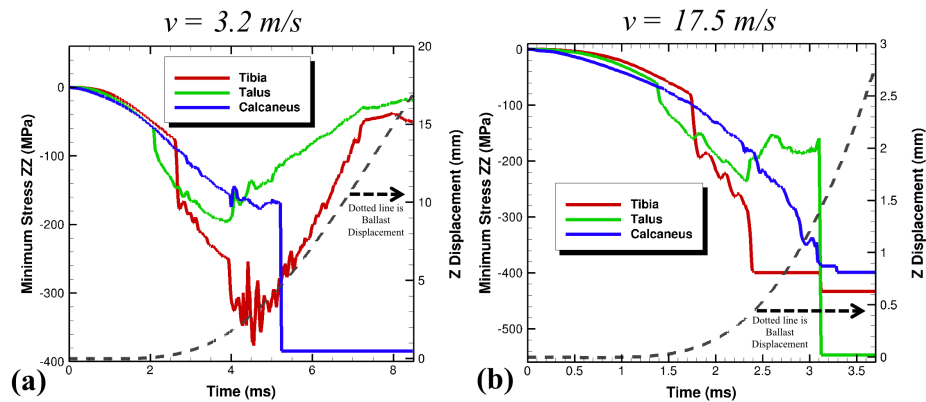


Figure 5: Maximum compressive stress in the axial direction as a function of time for case of (a) 3.2 and (b) 17.5 m/s.

Figure 6a and b shows the principal stresses in the plantar surface of the calcaneus and inferior

talus for case 1 and case 2, respectively. This is important to examine, considering the large amount of failure observed in these regions. One interesting aspect of the response is the presence of tension-compression components resulting from the combined loading in these regions. In the inferior talus the rate at which compressive stresses grow is faster than the growth rate for tensile stresses up to, approximately 2 ms into the transient when fracture initiates in the trabecular region of talus. At 2.6 ms the acceleration of the applied velocity boundary conditions reverses, thus displacements are still increasing in the axial direction, but the rate of displacement of the floor plate decreases with time. Case 2 shown in Figure 6b shows similarities in the loading of the inferior talus up to the time of initiation of fracture. It is important to keep in mind that at this time, rate dependent material properties of the bone deformation and fracture response are not incorporated into the model so any stiffening of the model response derives from inertial effects alone. By approximately 2.4 ms, fracture morphology shows severe comminution (Figure 4). An interesting aspect of the response is the rate at which fracture occurs at a given location. For example, as seen in Figure 6b, at approximately 3.6 ms the principal stress in the inferior talus rapidly grows until the critical stress,  $\sigma_c^t$ , is reached and the failure process begins to dissipate energy. The curves in Figures 6a and b represent data extracted from one particular region of the respective model components.

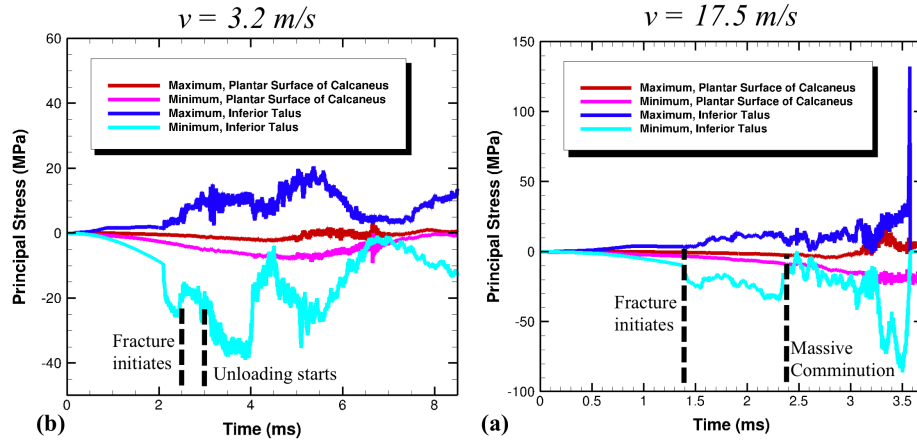


Figure 6: Principal stresses in the plantar surface of the calcaneus and inferior talus for both (a) case 1 and (b) case 2.

Figure 7 shows the damage predicted for the 17.5 m/s impact case at subsequent instants of the simulation transient. The color contours indicate if the damage is associated with tension or compression, and whether it is predicted to occur in the trabecular or cortical bone. Damage initiates in the talus and begins at approximately 1.45 ms. At 2.50 ms, a mix of trabecular and cortical bone failure is observed. For both loading conditions, mid-tibia failure is not observed, suggesting that direct axial loading for the lower extremity subjected to underbody blast mainly affects the ankle complex. However, the extrinsic effects such as lateral seat loading to the mid lower leg giving rise to off-axis loading may significantly alter the predicted fracture morphologies.

Once elements are fully damaged, they are removed from the simulation using the element deletion method. While primitive in approach, element deletion helps to keep the simulation numerically stable and also provides a simple and quick means to estimate damage. Figure 8 shows

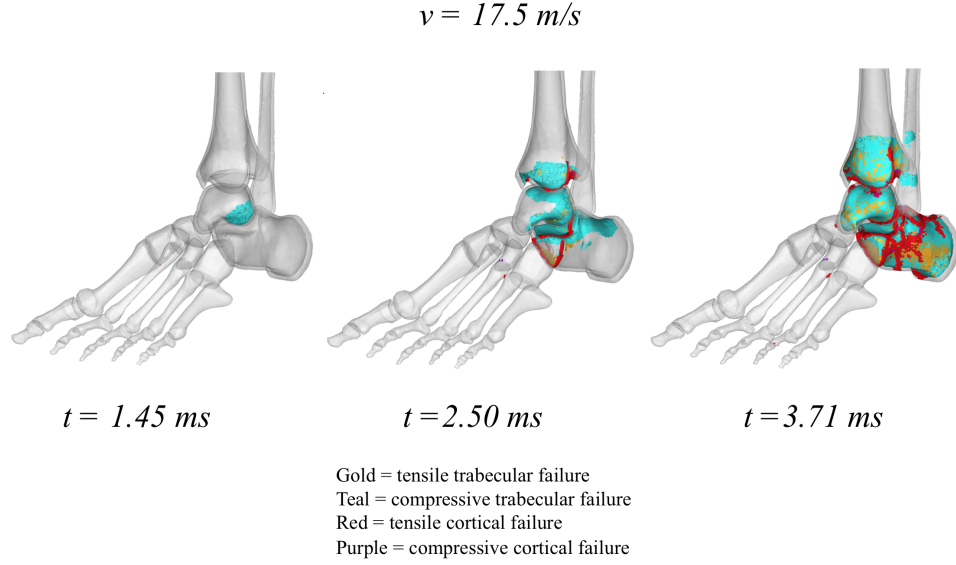


Figure 7: Damage predicted for the 17.5 m/s impact case over various times

the percentage of mass removed from the simulation for the talus, which is interesting to examine because this is where damage is first observed. This is not the most accurate means to evaluate damage, because this measure only accounts for elements fully damaged. In fact, many elements using the elastic-fracture model are in the “transition” phase of failure, dissipating energy associated with the unloading portion of the curve shown in Figure 2. For the 3.2 and 17.5 m/s cases, although the time scales of damage are different, similar amounts of mass are removed from both tensile and compression failure, i.e., 13 and 31.5 percent, respectively. However, for the 17.5 m/s case cortical failure is observed, whereas for the 3.2 m/s only trabecular failure in the talus was observed. This reveals an interesting aspect of lower extremity failure mechanisms directly relevant to the investigation of the injury process for sub-critical loading that cause no cortical failure. The cortical bone has higher strength and is thought to directly correlate with the ability of the lower extremities to carry load. The lower strength of the trabecular bone makes it vulnerable to dynamic, non-equilibrium stresses that can activate cracks. This is an important deviation from traditional biomechanics that tend to study the bone system in equilibrium when the response of the cortical shell is primarily responsible to determine the load bearing capacity of the structure.

## 4 Effect of Critical Crack Stretch Parameter

Since the approach used in this study is one that is mesh dependent, an initial parametric study was conducted to examine the effect of parameters used within the elastic fracture model. Figure 9 shows the maximum compressive principal stress predicted by the model plotted in terms of the tensile critical inelastic stretch,  $\epsilon_i$  for the 17.5 m/s loading condition. Also shown is the corresponding total mass removed from the system as a result. The predicted maximum compressive principal stress is diminished for low values of critical inelastic stretch. The smaller the critical stretch, the less energy is dissipated during the failure process, leading to more elements becoming



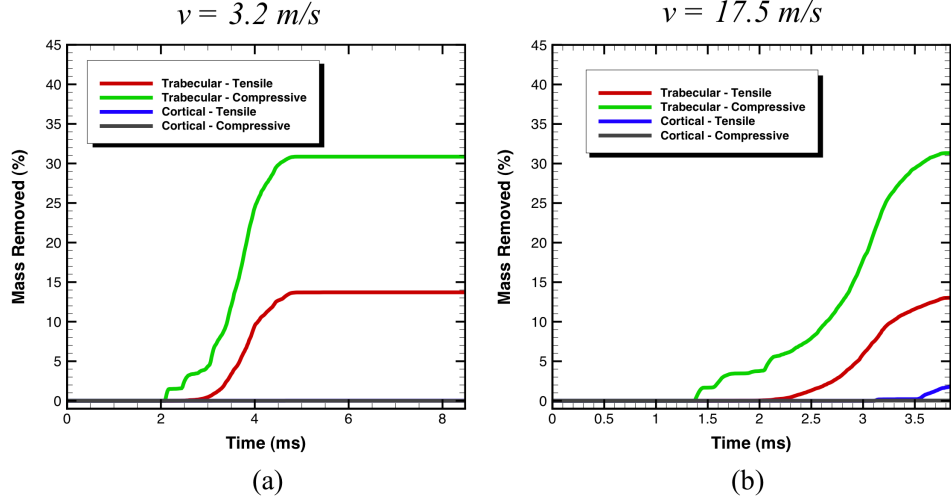
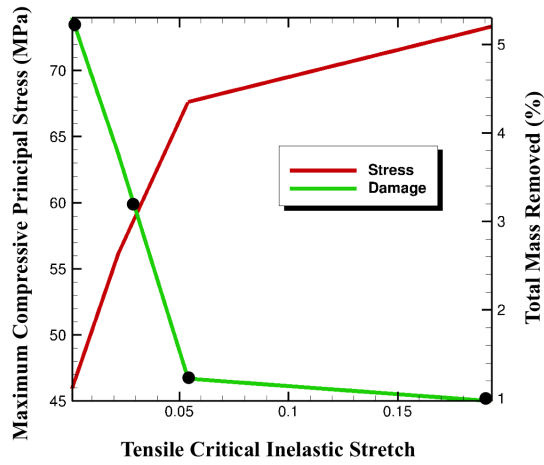


Figure 8: Percentage of mass removed from the simulation for talus for the (a) 3.2 m/s and (b) 17.5 m/s cases. The talus is interesting to examine because this is where damage is first observed.

fully damaged, or more total mass removed. A significant increase in maximum compressive principal stress occurs when the critical inelastic stretch is increased up to 0.05. Above this value of stretch, there seems to be a less dramatic effect on the principal stress and a lower effect on damage reduction. In terms of fracture surfaces, a lower fracture area is created with increasing inelastic stretch. In the future, we hope to modify the constitutive law to take into account the distribution of element length scales. This development will allow the model to account for a distribution of critical inelastic stretch values, thus reducing mesh dependency effects.

## 5 Conclusions and Future Work

This paper has described a research effort to develop a hierarchical modeling approach for the lower extremities subjected to military underbody blasts and has specifically focused on developing a finite element model of the lower extremities undergoing high strain rate blast-induced deformation. Computations highlight the importance of understanding the initiation, propagation and coalescence of bone fracture. At the assembly level, a lower leg consisting of many different tissues was developed and evaluated. Similar to past experimental research, we numerically observe calcaneal, talar, midfoot fractures, as well as ankle rotation before any tibia or fibula fracture is observed. This study has some considerable limitations including the simplistic approach used to study the fracture process, the material properties that neglected rate dependence effects, and a number of anatomic details that were not represented but may be important. In future work, components within the assembly, such as the tibia will be refined by using sub-scale models of trabecular bone at the microstructural level and will capture micro-fracture mechanisms at the trabecular level. For that purpose, we will make use of the Discontinuous Galerkin finite element method for the computational model [Radovitzky et al., 2011]. Furthermore, a visco-elastic, visco-plastic formulation for the constitutive response of cortical and trabecular bone [Johnson et al., 2010] will be implemented, to allow for rate effects in the deformation response of the tissue. To better un-



Damage at 3.28 ms for  
3.2 m/s case

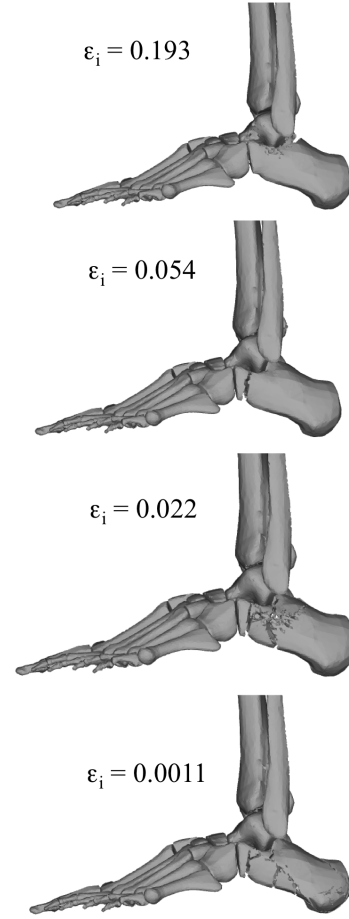


Figure 9: Maximum compressive principal stress plotted in terms of varying tensile critical inelastic stretch,  $\epsilon_i$  for the 17.5 m/s loading condition. Also shown is the corresponding total mass removed from the system as a result.

derstand how the open cellular structure of trabecular bone affects its macroscopic response and failure behavior, a meso-scale model will be developed. This hierarchical approach will be further extended to other model components to obtain a more accurate and biofidelic representation of the lower leg assembly.

## References

- C. Whitlock. Soaring IED attacks in afghanistan stymie u.s. counteroffensive, March 2010. URL <http://www.washingtonpost.com/wp-dyn/content/article/2010/03/17/AR2010031703649.html>. [Online; accessed 13-August-2010].
- D. J. Gabauer and H. C. Gabler. Acceleration-based occupant injury criteria for predicting injury in real-world crashes. *Biomedical Sciences Instrumentation*, 44:219–218, 2008.
- G. Nilakantan and A. Tabiei. Computational assessment of occupant injury caused by mine blasts underneath infantry vehicles. *International Journal of Vehicle Structures & Systems*, 1(1–3): 50–58, 2009. doi: {10.4273/ijvss.1.1-3.07}.
- NATO HFM-090, Task Group 25. Test methodology for protection of vehicle occupants against anti-vehicular landmine effects. Technical Report RTO-TR-HFM-090, NATO Research and Technology Organization, 2007.
- P. Manning, A. Wallace, C. Owen, A. Roberts, C. Oakley, and R. Lowne. Dynamic response and injury mechanism in the human foot and ankle and an analysis of dummy biofidelity. In *Proceedings of the 16th International Conference on Enhanced Safety of Vehicles*, pages 1960–1998, Canada, June 1998. Paper No.: 98-S9-O-11.
- J. R. Crandall, S. M. Kuppaa, G. S. Klopp, G. W. Hall, W. D. Pilkey, and S. R. Hurwitz. Mechanisms of injury and injury criteria for the human foot and ankle in dynamic axial impacts to the foot. *International Journal of Crashworthiness*, 3(2):147–162, 2003. URL <http://www.informaworld.com/10.1533/cras.1998.0068>.
- P. Begeman and N. Paravasthu. Static and dynamic compression loading of the lower leg. In *Proceedings of the 7th Injury Prevention Through Biomechanics Symposium*, Detroit, MI, 1997.
- S. Kuppaa, J. Wang, M. Haffner, and R. Eppinger. Lower extremity injuries and associated injury criteria. In *Proceedings of the 17th International Technical Conference on the Enhanced Safety of Vehicles*, National Highway Traffic Safety Administration, Washington, DC, 2001. Paper Number: 457.
- J. Manseau and M. Keown. Development of an assessment methodology for lower leg injuries resulting from anti-vehicular blast landmines. In Michael D. Gilchrist, editor, *IUTAM Symposium on Impact Biomechanics: From Fundamental Insights to Applications*, volume 124, pages 33–40. Springer, The Netherlands, 2005. ISBN 0-470-84699-2.
- F. A. Bandak, R. E. Tannous, and T. Toridis. On the development of an osseo-ligamentous finite element model of the human ankle joint. *International Journal of Solids and Structures*, 38(10–13):1681 – 1697, 2001. ISSN 0020-7683. doi: DOI:10.1016/S0020-7683(00)00129-3. URL <http://www.sciencedirect.com/science/article/pii/S0020768300001293>.
- N. Yoganandan, F.A Pinar, M. Boyton, and J. A. Sances. Biomechanics of foot and ankle fractures. In *In the Proceedings of the International Conference on Pelvic and Lower Extremity Injuries*, pages 201–209, 1995.

- N. Yoganandan, F.A Pinar, M. Boyton, P. Begeman, and P. Prasad. Dynamic axial tolerance of the human foot-ankle complex. In *In the Proceedings of 40th Stapp Car Crash Conference*, pages 207–218, 1996.
- J. Alvarez. Epidemiology of blast injuries in current operations. Technical Report RTO-EN-HFM-207, NATO Research and Technology Organization, 2011.
- T. Belytschko, W. K. Liu, and B. Moran. *Nonlinear Finite Elements for Continua and Structures*. John Wiley & Sons, LTD., New York, 2000.
- B. H. Thacker, W. L. Francis, and D. P. Nicolella. Model validation and uncertainty quantification applied to cervical spine injury assessment. In *Computational Uncertainty in Military Vehicle Design (pp. 26-1 26-30). Meeting Proceedings RTO-MP-AVT-147, Paper 26*, Neuilly-sur-Seine, France: RTO, 2007.
- S.J. Hall. *Basic biomechanics*. McGraw-Hill, 2006. ISBN 9780073044811.
- Jason Tak-Man Cheung, Ming Zhang, Aaron Kam-Lun Leung, and Yu-Bo Fan. Three-dimensional finite element analysis of the foot during standing a material sensitivity study. *Journal of Biomechanics*, 38(5):1045 – 1054, 2005. ISSN 0021-9290. doi: 10.1016/j.jbiomech.2004.05.035. URL <http://www.sciencedirect.com/science/article/pii/S0021929004002842>.
- Zygo Media Group, Inc., 2012. URL [www.3dscience.com](http://www.3dscience.com). [Online; accessed 28-March-2012].
- P. J. Schuster, C. C. Chou, P. Prasad, and G. Jayaraman. Development and validation of a pedestrian lower limb non-linear 3-d finite element model. *Stapp Car Crash Journal*, 44:215–334, 2000.
- Ani Ural, Peter Zioupos, Drew Buchanan, and Deepak Vashishth. The effect of strain rate on fracture toughness of human cortical bone: A finite element study. *Journal of the Mechanical Behavior of Biomedical Materials*, 4(7):1021 – 1032, 2011. ISSN 1751-6161. doi: 10.1016/j.jmbbm.2011.03.011. URL <http://www.sciencedirect.com/science/article/pii/S1751616111000567>.
- J.D. Currey. *Bones: structure and mechanics*. Princeton University Press, 2002. ISBN 9780691090962.
- R.B. Cook and P. Zioupos. The fracture toughness of cancellous bone. *Journal of Biomechanics*, 42(13):2054 – 2060, 2009. ISSN 0021-9290. doi: 10.1016/j.jbiomech.2009.06.001. URL <http://www.sciencedirect.com/science/article/pii/S0021929009003327>.
- MatWeb. Medium carbon steel, 2011.
- Jeong-Hoon Song, Hongwu Wang, and Ted Belytschko. A comparative study on finite element methods for dynamic fracture. *Computational Mechanics*, 42:239–250, 2008. ISSN 0178-7675. URL <http://dx.doi.org/10.1007/s00466-007-0210-x>. 10.1007/s00466-007-0210-x.
- M Donadon, L Iannucci, B Falzon, J Hodgkinson, and S Dealmeida. A progressive failure model for composite laminates subjected to low velocity impact damage. *Computers Structures*, 86(11-12):1232–1252, 2008. URL <http://linkinghub.elsevier.com/retrieve/pii/S0045794907002982>.

- M. Cervera and M. Chiumenti. Mesh objective tensile cracking via a local continuum damage model and a crack tracking technique. *Computer Methods in Applied Mechanics and Engineering*, 196(1–):304 – 320, 2006. ISSN 0045-7825. doi: 10.1016/j.cma.2006.04.008. URL <http://www.sciencedirect.com/science/article/pii/S0045782506001460>.
- L Iannucci and M L Willows. An energy based damage mechanics approach to modelling impact onto woven composite materials–part i: Numerical models. *Composites Part A Applied Science and Manufacturing*, 37(11):2041–2056, 2006.
- R. Radovitzky, A. Seagraves, M. Tupek, and L. Noels. A scalable 3d fracture and fragmentation algorithm based on a hybrid, discontinuous galerkin, cohesive element method. *Computer Methods in Applied Mechanics and Engineering*, 200(14):326 – 344, 2011. ISSN 0045-7825. doi: 10.1016/j.cma.2010.08.014. URL <http://www.sciencedirect.com/science/article/pii/S0045782510002471>.
- T.P.M. Johnson, S. Socrate, and M.C. Boyce. A viscoelastic, viscoplastic model of cortical bone valid at low and high strain rates. *Acta Biomaterialia*, 6(10):4073 – 4080, 2010. ISSN 1742-7061. doi: 10.1016/j.actbio.2010.04.017. URL <http://www.sciencedirect.com/science/article/pii/S1742706110002060>.

NO. OF COPIES	ORGANIZATION	NO. OF COPIES	ORGANIZATION
1 ELEC	ADMNSTR DEFNS TECHL INFO CTR ATTN DTIC OCP 8725 JOHN J KINGMAN RD STE 0944 FT BELVOIR VA 22060-6218	1	DIRECTOR UNIFORMED SERVICES UNIVERSITY OF THE HEALTH SCIENCES ATTN P RAPP
2	THE JOHNS HOPKINS UNIV APPLIED PHYSICS LAB ATTN R KRAFT ATTN A MERKLE	1	US ARMY ABERDEEN TEST CTR ATTN TEDT AT SLB A FOURNIER
2	MIT ATTN R RADOVITZKY ATTN S SOCRATE	1	US ARMED FORCES MEDICAL EXAMINER SYSTEM ATTN J GETZ
1	BAE SYSTEMS ATTN R TANNOUS	1	DEFENCE SCIENCE & TECH LAB PHYSICAL SCIENCES DEPT ATTN D POPE
1	WALTER REED NATIONAL MEDICAL CTR SPINE LABORATORY ATTN E WRIGHT	1	UNIVERSITY OF NEBRASKA ATTN N CHANDRA
3	US ARMY MEDICAL RSRCH INSTITUTE OF INFECTIOUS DISEASE ATTN MRMC RTB F LEBEDA ATTN MRMC RTB J USCILOWICZ ATTN MRMC RTB W LEI	1	MISSISSIPPI STATE UNIVERSITY ATTN L N WILLIAMS
3	US ARMY MEDICAL RSRCH AND MATL CMND ATTN MCMR RTB M J LEGGIERI ATTN MCMR RTB R GUPTA ATTN MCMR RTB R SHOGE	2	WAKE FOREST UNIVERSITY CENTER FOR INJURY BIOMECHANICS ATTN F SCOTT GAYZIK ATTN J STITZEL
2	AMC-TARDEC ATTN RDTA RS H PIETSCH ATTN RDTA RS R SCHERER	2	SOUTHWEST RESEARCH INSTITUTE MECHANICAL AND MATERIALS ENGINEERING DIV MATERIALS ENGINEERING DEPT ATTN D NICOLELLA ATTN W FRANCIS
7	NATICK SOLDIER RSRCH, DEV, AND ENGRG CTR ATTN AMSRD NSC WS TB J FITEK ATTN AMSRD NSC WS TB M CARBONI ATTN AMSSB-RIP-B(N) M MAFFEO ATTN RDNS D M CODEGA ATTN TSIP D LEE ATTN RSNS WSD J WARD ATTN AMSSB RIP P CUNNIFF	1	SANDIA NATL LABS ATTN MS 0836 S SCHUMACHER
		2	US ARMY AEROMEDICAL RSRCH LAB HENRY JACKSON FOUNDATION ATTN B MCENTYRE ATTN V CHANCEY
		1	JHU MECH ENG ATTN K T RAMESH
		1	JOHNS HOPKINS UNIVERSITY DEPT OF MECHANICAL ENGINEERING ATTN V NGUYEN

NO. OF COPIES	ORGANIZATION		
			ATTN RDRL WMP C J CLAYTON
			ATTN RDRL WMP C
			M GREENFIELD
1	DEPT OF BIOENGINEERING UNIV OF PENNSYLVANIA ATTN D MEANEY		ATTN RDRL WMP C
			M RAFTENBERG
			ATTN RDRL WMP C S BILYK
1	IMPERIAL BLAST BIOMECHANICS & BIOPHYSICS GROUP DEPT OF BIOENGINEERING IMPERIAL COLLEGE LONDON ATTN S D MASOUIROS		ATTN RDRL WMP C T W BJERKE
			ATTN RDRL WMP D J RUNYEON
			ATTN RDRL WMP D R DONEY
			ATTN RDRL WMP E P SWOBODA
			ATTN RDRL WMP F
			N GNIAZDOWSKI
1	SCHOOL OF MEDICINE DEPT OF ORTHOPEDIC SURGERY UNIV OF PITTSBURG ATTN P ALEXANDER		ATTN RDRL WMP
			S E SCHOENFELD
			ATTN RDRL WMP F R GUPTA
			ATTN RDRL WMP G S KUKUCK
			ATTN RDRL HRS C B LANCE
1	UNIV OF PITTSBURG ATTN W SCHNEIDER		ATTN RDRL HRS C K MCDOWELL
			ATTN RDRL HRS C K OIE
			ATTN RDRL HRS C W HAIRSTON
2	ENERGETICS TECHNOLOGY CENTER ATTN E MORITZ ATTN R KAVETSKY		ATTN RDRL SLB W A KULAGA
			ATTN RDRL SLB W C KENNEDY
			ATTN RDRL SLB W
			G ETTIENNE-MODESTE
			ATTN RDRL SLB W L ROACH
1	NAVAL AIR WARFARE CENTER-AIRCRAFT DIVISION ATTN B SHENDER		ATTN RDRL SLB W
			P FROUNFELKER
			ATTN RDRL SLB W R SPINK
			ATTN RDRL WMP C D DANDEKAR
			ATTN RDRL SLB W
1	CFD RESEARCH CORPORATION ATTN A PRZEKOWAS		W H MERMAGEN SR
			ATTN RDRL WMP F
			E FIORAVANTE
47	US ARMY RSRCH LAB ATTN RDRL WMP B S SATAPATHY ATTN RDRL SLB W N EBERIUS ATTN RDRL CIH C P CHUNG ATTN RDRL HRS C J VETTEL ATTN RDRL SL R COATES ATTN RDRL SLB W A BREUER ATTN RDRL SLB W P GILLICH ATTN RDRL WML H B SCHUSTER ATTN RDRL WMM B B LOVE ATTN RDRL WMP B Y HUANG ATTN RDRL WMP B A DAGRO ATTN RDRL WMP B C HOPPEL ATTN RDRL WMP B D CASEM ATTN RDRL WMP B D POWELL ATTN RDRL WMP B M LYNCH ATTN RDRL WMP B M SCHEIDLER ATTN RDRL WMP B P MCKEE ATTN RDRL WMP B S WOZNAK ATTN RDRL WMP B T WEERASOORIYA ATTN RDRL WMP C B LEAVY	3 PDF 1 HC	US ARMY RSRCH LAB ATTN IMAL HRA MAIL & RECORDS MGMT (1 HC) ATTN RDRL CIO LL TECHL LIB ATTN RDRL WMP F A FRYDMAN ATTN RDRL WMP F R KARGUS

INTENTIONALLY LEFT BLANK.